APPLIED PHYSICS

Experimental demonstration of acoustic semimetal with topologically charged nodal surface

Meng Xiao[1,2]*, Liping Ye[2]*, Chunyin Qiu[2†], Hailong He[2], Zhengyou Liu[2,3†], Shanhui Fan[1†]

Weyl points are zero-dimensional band degeneracy in three-dimensional momentum space that has nonzero topological charges. The presence of the topological charges protects the degeneracy points against perturbations and enables a variety of fascinating phenomena. It is so far unclear whether such charged objects can occur in higher dimensions. Here, we introduce the concept of charged nodal surface, a two-dimensional band degeneracy surface in momentum space that is topologically charged. We provide an effective Hamiltonian for this charged nodal surface and show that such a Hamiltonian can be implemented in a tight-binding model. This is followed by an experimental realization in a phononic crystal. The measured topologically protected surface arc state of such an acoustic semimetal reproduces excellently the full-wave simulations. Creating high-dimensional charged geometric objects in momentum space promises a broad range of unexplored topological physics.

INTRODUCTION

The study of topologically nontrivial states of matter has been attracting intensive interest in condensed matter physics as well as in optics and acoustics. Notable accomplishments include the discovery of the two-dimensional (2D) quantum spin Hall effect (1, 2) and, more recently, topological gapless semimetals (3). For 3D topological semimetals, the band degeneracy can occur at a point, line, or surface, as in Weyl semimetals and Dirac semimetals (4–21), nodal line semimetals (22–24), and nodal surface semimetals (25, 26), respectively. While a Weyl point is topologically charged in that it carries a nonzero quantized total Berry flux, nodal lines and surfaces themselves do not carry nonzero $\mathbb{Z}$ charge of Berry flux in all previous works (22–26). Exploring higher-dimensional topologically charged band degeneracy not only enriches the family of topological semimetals but may also enable the controlling of topological charges in a more flexible way and, hence, change the manifestations of associated phenomena, such as the chiral anomaly and negative magnetoresistance (27).

Here, we report the existence of a topologically charged nodal surface—a 2D band degeneracy in momentum space that carries nonzero total Berry flux. We first show that such a charged nodal surface exists in a tight-binding model. Motivated by the tight-binding model, we have designed a 3D airborne phononic crystal exhibiting twofold screw symmetry and experimentally revealed the existence of charged nodal surfaces through measuring the topological surface states. Substantial different from Weyl semimetals where the Fermi arcs (i.e., cut of the topological surface states at the Fermi energy) are pinned to Weyl points, here the ends of the surface state arcs depend sensitively on the surface truncation of the acoustic semimetal and thus provide a unique way to engineer the surface state arcs. Our result indicates that in the band theory, topologically charged objects are not restricted to zero dimension like Weyl points, and thus pointing to previously unexplored opportunities for the design of topological materials.

RESULTS

Model Hamiltonian of the charged nodal surface

In a 3D system, the total Berry flux through any closed surface is quantized and defines the first Chern number of the closed surface. When the Chern number is nonzero, there must be band degeneracy that carries the charge of Berry flux for a system with time reversal symmetry. Weyl points (4) are one class of such band degeneracy points with nonzero Berry charges. A simple Hamiltonian of the Weyl point with charge +1 can be written as

$$\hat{H} = q_x \sigma_x + q_y \sigma_y + q_z \sigma_z \tag{1}$$

where q_x, q_y, and q_z are three wave vector components measured from the Weyl point, and σ_x, σ_y, and σ_z are Pauli matrices. Figure 1A illustrates the Berry flux density emitted by the Weyl point, with a total Berry flux of 2π.

However, Weyl points are not the only kind of topologically charged geometric objects in momentum space. Here, we introduce a nodal surface that also carries a nonzero charge. A simple Hamiltonian of the charged nodal surface (with charge +1) is given by

$$\hat{H} = q_z(q_x \sigma_x + q_y \sigma_y) + q_z \sigma_z \tag{2}$$

The eigenvalues of the effective Hamiltonian, $E_{\pm} = \pm q_z \sqrt{1 + q_\rho^2}$ (with $q_\rho = \sqrt{q_x^2 + q_y^2}$), are degenerate at $q_z = 0$ and change linearly with q_z when away from the nodal surface, indicating the presence of a nodal surface (25, 26). The subscripts "+" and "−" correspond to the upper and lower bands, respectively. Analytically, the Hamiltonian in Eq. 2 gives rise to the Berry flux distribution of the nodal surface

$$\mathbf{B}_{\pm} = \mp \frac{1}{2\left(1 + q_\rho^2\right)^{3/2}} \hat{z} \tag{3}$$

which emits a Berry flux of 2π in total. As illustrated in Fig. 1B, now the Berry flux concentrates around $q_\rho = 0$ and decays quickly away from it. In contrast, the Berry flux of a Weyl point originates from a

[1]Department of Electrical Engineering, and Ginzton Laboratory, Stanford University, Stanford, CA 94305, USA. [2]Key Laboratory of Artificial Micro- and Nano-structures of Ministry of Education and School of Physics and Technology, Wuhan University, Wuhan 430072, China. [3]Institute for Advanced Studies, Wuhan University, Wuhan 430072, China.
*These authors contributed equally to this work.
†Corresponding author. Email: cyqiu@whu.edu.cn (C.Q.); zyliu@whu.edu.cn (Z.L.); shanhui@stanford.edu (S.F.)
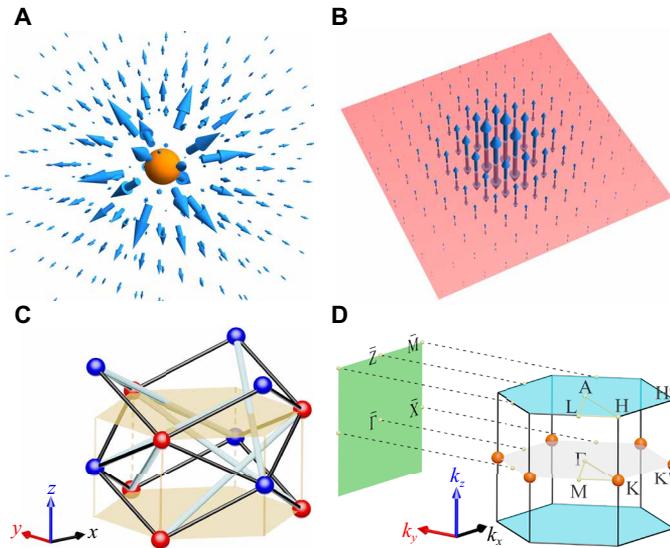
Fig. 1. Charged nodal surface and a tight-binding model realization. (**A**) Berry flux density distributions of a Weyl point. (**B**) The same as (A) but for a charged nodal surface. The orange sphere and transparent red plane indicate the Weyl point and nodal surface, respectively. The arrows represent the orientation and amplitude of the Berry flux density. (**C**) Sketch of the tight-binding model. Each unit cell consists of two sublattices (color spheres). Their projections onto the x-y plane form a hexagonal lattice with a lattice constant a. The lattice constant along the z direction is h, and the red and blue spheres are located on the planes $z = nh$ and $z = (n + 1/2)h$, respectively, with n being an integer. The cyan and black bonds represent hopping between different sites, associated with hopping strengths t_c and t_0, respectively. This model exhibits $\bar{C}_{2z}$ symmetry with broken inversion symmetry. (**D**) The first Brillouin zone and its projection onto the k_x-k_z plane. The orange spheres represent Weyl points with topological charges +1, and the cyan surfaces at $k_z = \pm \pi/h$ represent the nodal surfaces with charges −2.

singular point (the Weyl point) (Fig. 1A), even though they both have the same charge of Berry flux. Nodal surfaces can also have other integer charges of Berry flux, i.e., they belong to $\mathbb{Z}$ classification, as discussed in detail in section S1. Note that for a general form of the charged nodal surface, the Berry flux is no longer limited to the z direction as in Eq. 3.

Tight-binding model

The Hamiltonian of Eq. 2 can be embedded in a simple tight-binding model. The realizations of nodal surfaces protected by different symmetries have been theoretically discussed in very recent works (*24*–*26*). None of these works, however, showed a nodal surface that carries a nonzero $\mathbb{Z}$ charge of Berry flux. Here, we consider a system exhibiting both time reversal symmetry $\mathcal{T}$ and a twofold screw symmetry along the z direction $\tilde{C}_{2z}$. We define a compound anti-unitary symmetry operator $G_{2z} \equiv \mathcal{T}\tilde{C}_{2z}$, which, in real space, acts as

$$G_{2z} : (x, y, z, t) \mapsto (-x, -y, z + h/2, -t) \qquad (4)$$

Here, h represents the lattice constant along the z direction. It is easy to check that $G_{2z}^2 = -1$ for a Bloch wave function on the $k_z = \pi/h$ plane with arbitrary k_x and k_y, where k_x, k_y, and k_z are the wave vectors along the x, y, and z directions, respectively. Therefore, $k_z = \pi/h$ forms a nodal surface due to a Kramers degeneracy on this surface (*26*). We emphasize here that nodal surface being protected by G_{2z}

is a symmetry argument only and does not depend on the detailed form of the Hamiltonian. To further construct a charged nodal surface, one has to break either the inversion symmetry or time reversal symmetry or both to achieve a nonzero Berry flux (*28*). Therefore, the idea to construct a charged nodal surface is to consider a system with G_{2z} symmetry and properly break inversion or time reversal symmetry to get the nodal surface charged. In this work, we implement inversion symmetry breaking.

Figure 1C shows a simple tight-binding model with G_{2z} symmetry. Two sublattices (red and blue spheres) are located on the $z = 0$ and $z = h/2$ planes. When projected to the x-y plane, the two sublattices are respectively projected to the A and B sites of a hexagonal lattice with a lattice constant a. There is a coupling t_c (cyan bond) between neighboring A (or B) sites and a coupling t_0 (black bond) between neighboring A and B sites. Both t_c and t_0 are real, as required by time reversal symmetry. In addition, this system exhibits G_{2z} symmetry and breaks inversion symmetry. According to the above analysis, this tight-binding model should have a nodal surface at $k_z = \pi/h$. This is confirmed by the calculated band structure (see section S2).

In addition to the nodal surface, we also note the existence of Weyl points at the K and K′ points of the bulk Brillouin zone. The charges of these two Weyl points are identical due to time reversal symmetry. Since the total charges inside the Brillouin zone must vanish (*29*), the charges of Weyl points must be compensated by the charge of the nodal surface, as these points and the nodal surface are the only band-degenerate features in the Brillouin zone. Hence, we conclude that the nodal surface here should also be charged. This has been directly verified by calculating the Chern number (see section S2). The charge distribution of this tight-binding model with $t_c = -0.1$ and $t_0 = -0.6$ is shown schematically in Fig. 1D, where the orange spheres and the cyan surface label the Weyl points and nodal surface with charges +1 and −2, respectively. As mentioned above, the Berry flux of a nodal surface actually concentrates around some special points in the momentum space (Fig. 1B). In this tight-binding model, the Berry flux of the nodal surface can be well captured by two charge −1 nodal surface Hamiltonians located at $H \equiv (4\pi/3a, 0, \pi/h)$ and $H' \equiv (-4\pi/3a, 0, \pi/h)$, respectively. To see this point, we expand the Hamiltonian near H and H′ with respect to q_x, q_y, and q_z, and keeping to the lowest order, the Hamiltonian becomes

$$\hat{H} = 3t_c \mathbf{I} + \frac{\sqrt{3}}{2} [aht_0 q_z (\pm q_x \sigma_x - q_y \sigma_y) \mp 6ht_c q_z \sigma_z] \qquad (5)$$

where (q_x, q_y, q_z) represent the wave vector measured from H or H′, $\mathbf{I}$ is the 2×2 identity matrix, and the upper and lower signs represent the Hamiltonian near H and H′ points, respectively. Equations 5 and 2 share a similar form up to some constants and a unit matrix. We, hence, conclude that the total charge of the nodal surface is $2 \, \mathrm{sgn}(t_c)$, which is independent of t_0. It is worth pointing out that for a more general system beyond the above tight-binding model, G_{2z} symmetry only protects the presence of a nodal surface at $k_z h = \pi$ and does not guarantee the existence of nonzero charge. In section S3, we demonstrate a topological phase transition, where a nodal surface changes its charge by emitting or absorbing an integer number of Weyl points, through controlling the strength of the next nearest layer couplings. We also note that the nodal surface is stably charged before this topological transition, provided that G_{2z} symmetry is preserved.

Acoustic semimetal with a charged nodal surface

The tight-binding model can be implemented directly in a physical structure, as we have shown in (30). We note that the charged nodal surface is not limited to the tight-binding model. To simplify the experimental demonstration, below we show that a suitably designed 3D phononic crystal can host a charged nodal surface. Figure 2A shows the unit cell geometry of this phononic crystal, in which the solid ingredient (colored) is designed fully connected for the convenience of practical sample fabrication. The phononic crystal is arranged by a hexagonal lattice in the x-y plane and has a spatial symmetry $\tilde{C}_{2z}$ as required. In particular, the slanted cyan cylinders are used to break the inversion symmetry. Figure 2B presents the bulk band structure of the crystal along several high symmetry directions of the reciprocal space (see Fig. 1D). We focus on the lowest two bands. As expected, double degeneracy emerges in the whole momentum surface $k_z = \pi/h$, of which the degenerate bands split linearly (e.g., see Γ-A direction). The degenerate bands are very flat, which spans from 9.75 to 9.79 kHz. Similar to the tight-binding model, in addition to the nodal surface, a node point of frequency 9.43 kHz is observed at K (K′) point, around which the dispersion curves are linear in all directions. Our further calculations confirm that the charge distributions of the Weyl points and the nodal surface are the same as the above tight-binding model (as labeled in Fig. 1D). The lowest two bands are isolated from higher ones, which facilitate the experimental detection of the topologically nontrivial surface states. To further confirm the topological nature of the nodal surface, we consider a phononic crystal slab of finite thickness along the y direction and calculate the in-plane dispersions for the slab surfaces XZ$_1$ and XZ$_2$ imposed with rigid boundary conditions. The detailed surface truncations are specified in Fig. 2C (right panel). As exemplified by the momentum $k_z = 0.5\pi/h$, the in-plane dispersion of the slab (Fig. 2C, left panel) exhibits one gapless one-way edge mode for each of the XZ$_1$ and XZ$_2$ surfaces. As there is no other band degeneracy except for the Weyl point and the nodal surface, the existence of topological edge states justifies the nontrivial topology of the nodal surface.

Experimental demonstrations

The topologically nontrivial surface states are confirmed in our airborne sound experiments. Figure 3A shows the experimental setup.

The phononic crystal slab has been fabricated precisely by 3D printing technique. Additional hard cover plates are integrated on the XZ$_1$ and XZ$_2$ surfaces to emulate the rigid boundary conditions involved in our full-wave simulations. Note that the XZ$_1$ and XZ$_2$ surfaces cannot be related by the spatial symmetry and thus offer two comparative surface dispersions measured from a single sample. To excite and detect the pressure distribution on a given surface, a rectangular lattice of circular holes has been perforated through the cover plate. A point-like sound source is positioned at the bottom left corner of the sample surface (see Materials and Methods), which excite mostly the states propagating toward the top and right. This treatment gives a relatively long distance of sound propagation and relaxes the finite size effect to some extent. During our measurement, all the holes on the substrate are sealed except for the one reserved for the sound probe. By Fourier transforming the measured surface field, we can map out the in-plane dispersion at any desired frequency. Figure 3B shows the dispersions for the XZ$_1$ surface, measured at the frequencies of Weyl point (9.43 kHz, left panel) and nodal surface (9.75 kHz, right panel). In addition to the projected bulk bands (gray regions), the measured surface arcs (bright color), on which the surface acoustic states carry specific propagation directions (labeled by arrows), agree well with those simulation results (white curves) for both frequencies. The band broadening comes from the finite size effect. Similar agreements are also observed in Fig. 3C for the XZ$_2$ surface. Note that this new surface allows the presence of some additional topologically trivial surface states (black curves) near the surface Brillouin zone boundary $k_z = \pi/h$. Comparing Fig. 3B with Fig. 3C, both the topological surface arcs start from the projection of Weyl point at 9.43 kHz but end by apparently different momenta at the nodal surface frequency 9.75 kHz. This points out a major difference from Weyl semimetals, wherein the Fermi arcs are always pinned at the projection of the Weyl points independent of the boundary condition. In contrast, the Fermi arcs in our system connect the projections of the Weyl points and the nodal surface. The end point of the Fermi arc on the nodal surface can shift depending on the boundary condition. Last, in Fig. 3D, we present the measured frequency dispersions for $k_z = 0.5\pi/h$ in the bulk gap, which reproduce well the numerical data for both surfaces again and demonstrate the one-way property of these chiral edge states (10, 14).
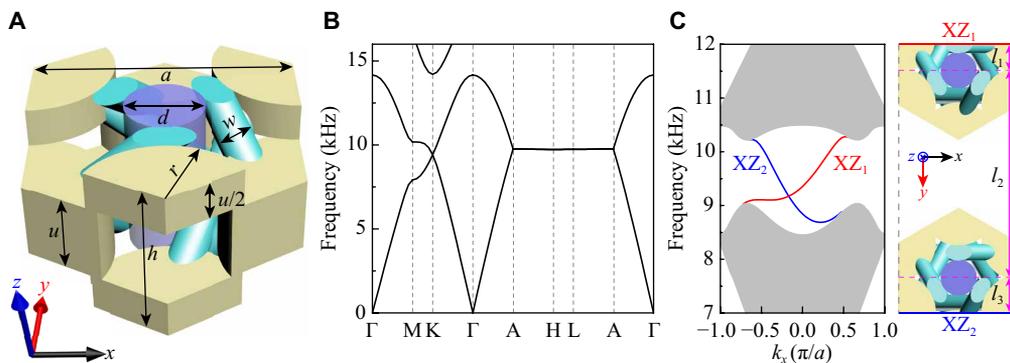
Fig. 2. A 3D phononic crystal designed with a charged nodal surface. (**A**) Unit cell geometry of the phononic crystal. The solid ingredient (colored) is acoustically rigid for airborne sound. The structure parameters are $a = 16.0$ mm, $h = 2u = 9.6$ mm, $r = 5.0$ mm, $d = 4.8$ mm, and $w = 2.2$ mm. (**B**) Bulk band structure simulated along several high symmetry directions of the first Brillouin zone. (**C**) Left: Gapless surface dispersions (color lines) for a phononic slab periodic in the x-z plane but finite along the y direction (see the right), simulated at a fixed $k_z = 0.5\pi/h$. The shadow regions are projected from the bulk bands. Right: Schematic view of the phononic crystal slab specified with truncation details for both the surfaces XZ$_1$ and XZ$_2$, where $l_1 = (d + w)/2$ and $l_3 = a/2\sqrt{3}$. Note that $l_2 = 5\sqrt{3}\,a$, and thus, the slab has a thickness more than five structural periods along the y direction.
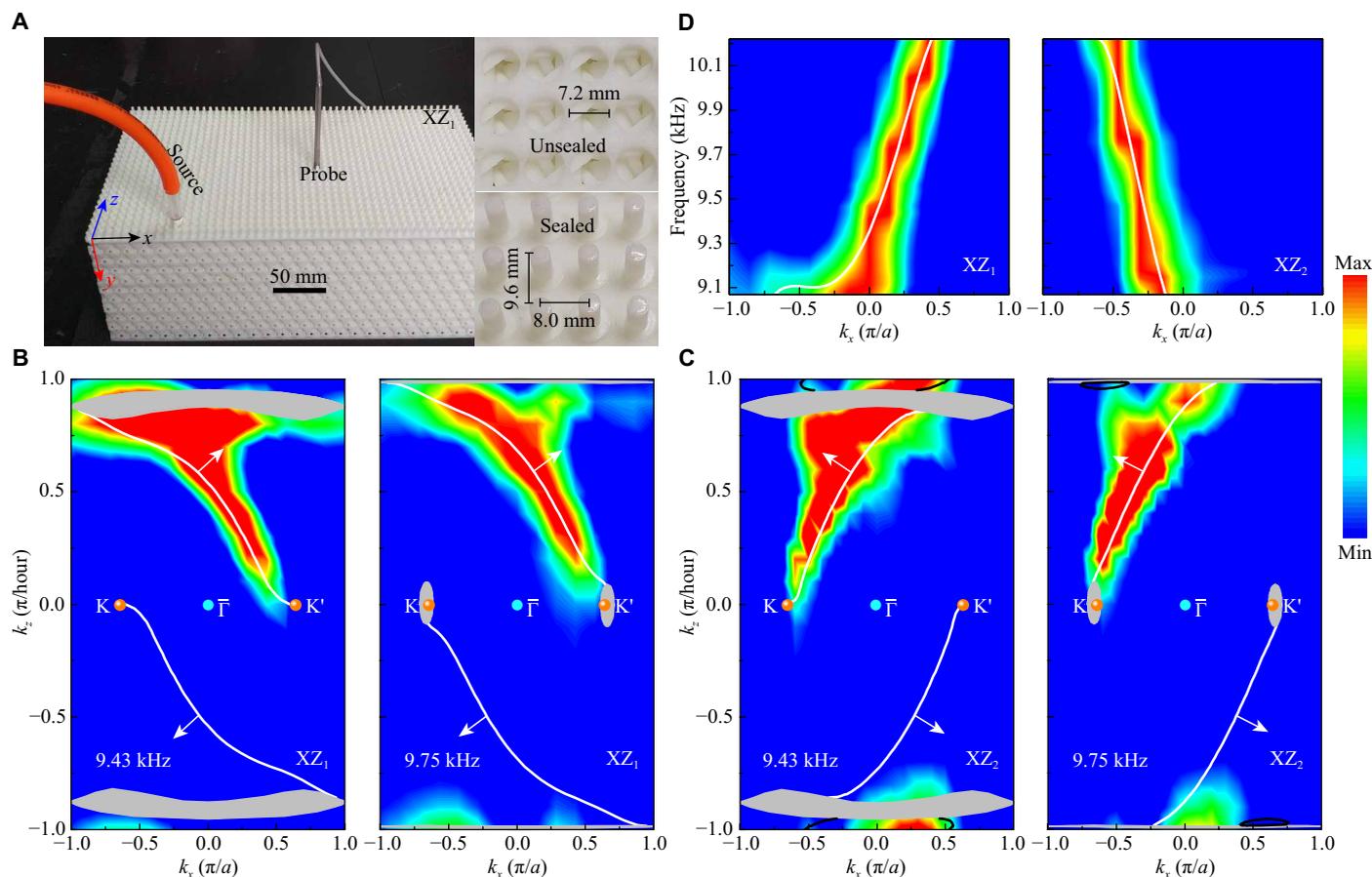
Fig. 3. Experimental detection of the topological surface states. (**A**) An image of the experimental setup. The insets give the details for the cover plate with holes opened (top) or sealed (bottom). The plugs that seal the holes will be removed one by one during the measurement. Photo credit: Liping Ye, Key Laboratory of Artificial Micro- and Nano-structures of Ministry of Education and School of Physics and Technology, Wuhan University. (**B**) The measured in-plane dispersions (bright color) for the XZ_1 surface, in good agreement with the simulated surface arcs (white curves) and bulk band projections (gray regions). The orange spheres label the projected Weyl points K and K', and the arrows indicate the main propagating directions of the surface acoustic waves. Note that 9.43 kHz corresponds to the Weyl point frequency, and 9.75 kHz falls into the frequency range of the nodal surface. Since the (bulk) nodal surface bands are flat, their projections are narrow for 9.75 kHz. (**C**) The same as (B) but measured for the XZ_2 surface. Trivial surface states (black curves) appear in this case. (**D**) Experimentally measured surface dispersions (bright color) at $k_z = 0.5\pi/h$ for the sample surfaces XZ_1 and XZ_2, which reproduce excellently the simulation results (white curves).

DISCUSSION

In summary, this work has introduced the concept of charged nodal surface, a new type of geometric object in momentum space that carries $\mathbb{Z}$ charge of Berry flux. The consequent topologically protected surface states have been experimentally demonstrated by a 3D acoustic semimetal that works for audible airborne sound. Connected but distinct from our work, previous works have shown the existence of $\mathbb{Z}_2$ (*22, 31, 32*), $\mathbb{Z}_2 \oplus 2\mathbb{Z}$, or $\mathbb{Z}_2 \oplus \mathbb{Z}_2$ (*24*) charges for nodal line or nodal surface, but these charges are different from the $\mathbb{Z}$ charge of Berry flux we report here. The charged nodal surface discussed in our acoustic semimetal can also be realized in electronic and electromagnetic systems as well. Moreover, our work also indicates the possibility of a charged nodal line and points to abundant unexplored features of phenomena associated with the topological charges such as chiral anomaly and negative magneto-resistance (*27*).

Note added: When this work is under review, we become aware of a few interesting works discussing nodal surface in the electronic systems (*33–35*).

MATERIALS AND METHODS
Simulations

All simulations were implemented by a commercial solver package (COMSOL Multiphysics). The photosensitive resin used for 3D printing was modeled as acoustically rigid, considering its huge impedance contrast to the air background. The sound speed in air was taken as 340 m/s for room temperature 15°C. The 3D bulk band structure (Fig. 2B) was simulated by imposing Bloch boundary conditions in all directions. To calculate the k_z-fixed surface dispersions for a phononic crystal slab of finite thickness (Fig. 2C), rigid boundary conditions were used for its XZ_1 and XZ_2 surfaces, whereas Bloch boundary condition was applied to the x and z directions. The thickness of the phononic crystal slab and its detailed surface truncations were specified in Fig. 2C. In addition to the projected bulk bands, surface bands were attained for both the surfaces simultaneously, which can be distinguished from bulk bands by examining the field distributions. Similarly, the equifrequency contours of the surface acoustic states (Fig. 3, B and C) were extracted by scanning the whole surface Brillouin zone.

Experiments

Our experiment was performed for airborne sound at audible frequency. The controllable structure design and the less demanding signal detection enabled our macroscopic system to be an exceptional platform to probe the topological effect. The experimental sample, fabricated precisely by 3D printing technique, had sizes of 416.0, 146.7, and 240.0 mm along the x, y, and z directions, respectively. The covering substrate had a thickness of 2.0 mm. To excite the surface arc states, a broadband point–like sound source, launched from a tube with radius ~3.5 mm, was inserted inside a hole near the bottom left of the sample (Fig. 3A). (The sound source was positioned according to the group velocity information through calculating the equifrequency contours of the topologically nontrivial surface acoustic states. It was confirmed that if the source was located at the top right of the sample, the surface arc states propagating toward the lower left direction would be excited, which serves as a measurement of the complementary surface arcs exhibited in Fig. 3.) The localized surface field was detected hole by hole through a portable microphone with radius ~3.5 mm (B&K Type 4187). The scanning steps were 8.0 and 9.6 mm along the x and z directions, respectively. The amplitude and phase information of the pressure field was recorded by a multi-analyzer system (B&K Type 3560B). The 2D Fourier transformation was performed for the measured pressure field to map out the surface dispersions (Fig. 3, B and C) at a given frequency. This further gave the experimental frequency spectra for any fixed k_z (Fig. 3D).

SUPPLEMENTARY MATERIALS

Supplementary material for this article is available at http://advances.sciencemag.org/cgi/content/full/6/8/eaav2360/DC1

Supplementary Text
Section S1. Nodal surfaces with higher charges
Section S2. Tight-binding model
Section S3. Transition between topologically nontrivial and trivial nodal surfaces
Fig. S1. Tight-binding model.
Fig. S2. Chern number as a function of k_z.
Fig. S3. Topological charge distributions before and after the topological transition.
Movie S1. Topological transition process.
References (36–40)

REFERENCES AND NOTES

1. X.-L. Qi, S.-C. Zhang, Topological insulators and superconductors. *Rev. Mod. Phys.* **83**, 1057–1110 (2011).
2. M. Z. Hasan, C. L. Kane, Colloquium: Topological insulators. *Rev. Mod. Phys.* **82**, 3045–3067 (2010).
3. A. A. Burkov, Topological semimetals. *Nat. Mater.* **15**, 1145–1148 (2016).
4. H. Weyl, Elektron und Gravitation. I. *Z. Phys.* **56**, 330–352 (1929).
5. X. Wan, A. M. Turner, A. Vishwanath, S. Y. Savrasov, Topological semimetal and Fermi-arc surface states in the electronic structure of pyrochlore iridates. *Phys. Rev. B* **83**, 205101 (2011).
6. S.-Y. Xu, I. Belopolski, N. Alidoust, M. Neupane, G. Bian, C. Zhang, R. Sankar, G. Chang, Z. Yuan, C.-C. Lee, S.-M. Huang, H. Zheng, J. Ma, D. S. Sanchez, B. Wang, A. Bansil, F. Chou, P. P. Shibayev, H. Lin, S. Jia, M. Z. Hasan, Discovery of a Weyl fermion semimetal and topological Fermi arcs. *Science* **349**, 613–617 (2015).
7. B. Q. Lv, H. M. Weng, B. B. Fu, X. P. Wang, H. Miao, J. Ma, P. Richard, X. C. Huang, L. X. Zhao, G. F. Chen, Z. Fang, X. Dai, T. Qian, H. Ding, Experimental discovery of Weyl semimetal TaAs. *Phys. Rev. X* **5**, 031013 (2015).
8. L. Lu, L. Fu, J. D. Joannopoulos, M. Soljačić, Weyl points and line nodes in gyroid photonic crystals. *Nat. Photonics* **7**, 294–299 (2013).
9. L. Lu, Z. Wang, D. Ye, L. Ran, L. Fu, J. D. Joannopoulos, M. Soljačić, Experimental observation of Weyl points. *Science* **349**, 622–624 (2015).
10. W.-J. Chen, M. Xiao, C. T. Chan, Photonic crystals possessing multiple Weyl points and the experimental observation of robust surface states. *Nat. Commun.* **7**, 13038 (2016).
11. M. Xiao, W.-J. Chen, W.-Y. He, C. T. Chan, Synthetic gauge flux and Weyl points in acoustic systems. *Nat. Phys.* **11**, 920–924 (2015).
12. M. Xiao, Q. Lin, S. Fan, Hyperbolic Weyl point in reciprocal chiral metamaterials. *Phys. Rev. Lett.* **117**, 057401 (2016).
13. W. Gao, B. Yang, M. Lawrence, F. Fang, B. Béri, S. Zhang, Photonic Weyl degeneracies in magnetized plasma. *Nat. Commun.* **7**, 12435 (2016).
14. Z. K. Liu, B. Zhou, Y. Zhang, Z. J. Wang, H. M. Weng, D. Prabhakaran, S.-K. Mo, Z. X. Shen, Z. Fang, X. Dai, Z. Hussain, Y. L. Chen, Discovery of a three-dimensional topological dirac semimetal, Na₃Bi. *Science* **343**, 864–867 (2014).
15. Z. Wang, Y. Sun, X.-Q. Chen, C. Franchini, G. Xu, H. Weng, X. Dai, Z. Fang, Dirac semimetal and topological phase transitions in A_3Bi (A=Na, K, Rb). *Phys. Rev. B* **85**, 195320 (2012).
16. J. Noh, S. Huang, D. Leykam, Y. D. Chong, K. P. Chen, M. C. Rechtsman, Experimental observation of optical Weyl points and Fermi arc-like surface states. *Nat. Phys.* **13**, 611–617 (2017).
17. F. Li, X. Huang, J. Lu, J. Ma, Z. Liu, Weyl points and Fermi arcs in a chiral phononic crystal. *Nat. Phys.* **14**, 30–34 (2018).
18. B. Yang, Q. Guo, B. Tremain, R. Liu, L. E. Barr, Q. Yan, W. Gao, H. Liu, Y. Xiang, J. Chen, C. Fang, A. Hibbins, L. Lu, S. Zhang, Ideal Weyl points and helicoid surface states in artificial photonic crystal structures. *Science* **359**, 1013–1016 (2018).
19. H. He, C. Qiu, L. Ye, X. Cai, X. Fan, M. Ke, F. Zhang, Z. Liu, Topological negative refraction of surface acoustic waves in a Weyl phononic crystal. *Nature* **560**, 61–64 (2018).
20. Z. Yang, B. Zhang, Acoustic type-II Weyl nodes from stacking dimerized chains. *Phys. Rev. Lett.* **117**, 224301 (2016).
21. Q. Lin, M. Xiao, L. Yuan, S. Fan, Photonic Weyl point in a two-dimensional resonator lattice with a synthetic frequency dimension. *Nat. Commun.* **7**, 13731 (2016).
22. C. Fang, Y. Chen, H.-Y. Kee, L. Fu, Topological nodal line semimetals with and without spin-orbital coupling. *Phys. Rev. B* **92**, 081201 (2015).
23. A. A. Burkov, M. D. Hook, L. Balents, Topological nodal semimetals. *Phys. Rev. B* **84**, 235126 (2011).
24. T. Bzdušek, M. Sigrist, Robust doubly charged nodal lines and nodal surfaces in centrosymmetric systems. *Phys. Rev. B* **96**, 155105 (2017).
25. C. Zhong, Y. Chen, Y. Xie, S. A. Yang, M. L. Cohen, S. B. Zhang, Towards three-dimensional Weyl-surface semimetals in graphene networks. *Nanoscale* **8**, 7232–7239 (2016).
26. Q.-F. Liang, J. Zhou, R. Yu, Z. Wang, H. Weng, Node-surface and node-line fermions from nonsymmorphic lattice symmetries. *Phys. Rev. B* **93**, 085427 (2016).
27. X. Huang, L. Zhao, Y. Long, P. Wang, D. Chen, Z. Yang, H. Liang, M. Xue, H. Weng, Z. Fang, X. Dai, G. Chen, Observation of the chiral-anomaly-induced negative magnetoresistance in 3D Weyl semimetal TaAs. *Phys. Rev. X* **5**, 031023 (2015).
28. L. Lu, J. D. Joannopoulos, M. Soljačić, Topological photonics. *Nat. Photonics* **8**, 821–829 (2014).
29. H. B. Nielsen, M. Ninomiya, Absence of neutrinos on a lattice: (II). Intuitive topological proof. *Nucl. Phys. B* **193**, 173–194 (1981).
30. M. Xiao, S. Fan, Topologically Charged Nodal Surface. arXiv:1709.02363 (2017).
31. K. Li, C. Li, J. Hu, Y. Li, C. Fang, Dirac and nodal line magnons in three-dimensional antiferromagnets. *Phys. Rev. Lett.* **119**, 247202 (2017).
32. D. F. Agterberg, P. M. R. Brydon, C. Timm, Bogoliubov Fermi surfaces in superconductors with broken time-reversal symmetry. *Phys. Rev. Lett.* **118**, 127001 (2017).
33. O. Türker, S. Moroz, Weyl nodal surfaces. *Phys. Rev. B* **97**, 075120 (2018).
34. W. Wu, Y. Liu, S. Li, C. Zhong, Z. M. Yu, X.-L. Sheng, Y. X. Zhao, S. A. Yang, Nodal surface semimetals: Theory and material realization. *Phys. Rev. B* **97**, 115125 (2018).
35. G. Chang, B. J. Wieder, F. Schindler, D. S. Sanchez, I. Belopolski, S.-M. Huang, B. Singh, D. Wu, T.-R. Chang, T. Neupert, S.-Y. Xu, H. Lin, M. Z. Hasan, Topological quantum properties of chiral crystals. *Nat. Mater.* **17**, 978–985 (2018).
36. C. Fang, M. J. Gilbert, X. Dai, B. A. Bernevig, Multi-Weyl topological semimetals stabilized by point group symmetry. *Phys. Rev. Lett.* **108**, 266802 (2012).
37. Y. Hatsugai, Chern number and edge states in the integer quantum Hall effect. *Phys. Rev. Lett.* **71**, 3697–3700 (1993).
38. A. H. Castro Neto, F. Guinea, N. M. R. Peres, K. S. Novoselov, A. K. Geim, The electronic properties of graphene. *Rev. Mod. Phys.* **81**, 109–162 (2009).
39. L. Yuan, M. Xiao, S. Fan, Time reversal of a wave packet with temporal modulation of gauge potential. *Phys. Rev. B* **94**, 140303(R) (2016).
40. R. Fleury, A. B. Khanikaev, A. Alù, Floquet topological insulators for sound. *Nat. Commun.* **7**, 11744 (2016).

developed the tight-binding model. L.Y. and C.Q. proposed the numerical system and did the experiments. M.X., C.Q., Z.L., and S.F. supervised the project. M.X., C.Q., L.Y., Z.L., and S.F. wrote the manuscript. All the authors contributed to the analysis and discussion of the results. **Competing interests:** The authors declare that they have no competing interests. **Data and materials availability:** All data needed to evaluate the conclusions in the paper are presented in the paper and/or the Supplementary Materials. Additional data related to this paper may be requested from the authors.

Science Advances

Experimental demonstration of acoustic semimetal with topologically charged nodal surface

Meng Xiao, Liping Ye, Chunyin Qiu, Hailong He, Zhengyou Liu and Shanhui Fan

ARTICLE TOOLS	http://advances.sciencemag.org/content/6/8/eaav2360
SUPPLEMENTARY MATERIALS	http://advances.sciencemag.org/content/suppl/2020/02/14/6.8.eaav2360.DC1
REFERENCES	This article cites 39 articles, 4 of which you can access for free http://advances.sciencemag.org/content/6/8/eaav2360#BIBL
PERMISSIONS	http://www.sciencemag.org/help/reprints-and-permissions

Use of this article is subject to the Terms of Service